SSI-91-FR

FINAL REPORT

DEVELOPMENT OF A SOURCE
OF VACUUM ULTRAVIOLET
AND SOFT X-RADIATION

National Aeronautics and Space Administration
Goddard Space Flight Center
Greenbelt, Maryland

N66-12612
(ACCESSION NUMBER)   (THRU)
54
(PAGES)   (CODE)
CR 68225
(NASA CR OR TMX OR AD NUMBER)   (CATEGORY)

GPO PRICE $ _____

CFSTI PRICE(S) $ _____

Hard copy (HC) ___3.00___

Microfiche (MF) ___.50___

ff 653 July 65

Prepared under Contract NAS 5-3365

ACE SCIENCES INCORPORATED

301 BEAR HILL ROAD, WALTHAM, MASS.

THE DEVELOPMENT OF A SOURCE OF
VACUUM ULTRAVIOLET AND SOFT
X-RADIATION

M . Doctoroff and J. Proud

Contract Number

NAS 5-3365

Prepared For

National Aeronautics and Space Administration
Goddard Space Flight Center
Greenbelt, Maryland

SCIENCES INCORPORATED

ABSTRACT

This report describes the successful development of an intense pulsed source of vacuum ultraviolet and soft x-radiation. The technique employed involves the compression of a helium plasma whose temperature is believed to be near 50 electron volts ($= kT$). Data are presented which show the shape of the x-ray pulse, and the spectra which can be expected from a finished prototype of the source being fabricated for delivery to Goddard Space Flight Center.

TABLE OF CONTENTS

TABLE OF FIGURES

TABLE OF FIGURES

SCIENCES INCORPORATED

THE DEVELOPMENT OF A SOURCE OF
VACUUM ULTRAVIOLET AND SOFT X-RADIATION

1. Introduction

This report describes the development of an intense pulsed source of vacuum ultraviolet radiation in the wavelength range 20 to 1000 Angstroms. The technique which has been employed involves the compression of a helium plasma whose temperature is believed to be near 50 electron volts $(= kT)$. During the compression period (several microseconds) the plasma emits line spectra from excited species as well as a continuum from recombination and bremsstrahlung.

The success of the development has been established by two methods of monitoring the UV spectrum. In one, the undispersed spectrum below about 1000 Angstroms has been observed by a fluor-photomultiplier method. In the second, a small vacuum spectrograph has been employed. The spectra obtained include a multitude of emission lines in the wavelength range between 100 and 400 Angstroms. The line spectrum originates not only from helium but also from highly ionized contaminants in the plasma compression.

In addition to the results of the research which are reported herein, a finished prototype of the source is being fabricated for delivery to Goddard Space Flight Center. This device contains many engineering refinements based on the experience gained in the research program and is designed to mate to the JACO Ultraviolet Spectrometer at the Center. While some of the operational characteristics of the finished device are included here, a separate manual of operation is also being prepared.

Section 2 discusses the theoretical considerations which constitute the logical basis for this project. Here, the theory is described to illustrate the use of a plasma compression for producing the radiation,

SCIENCES INCORPORATED

and the quantities of radiation are estimated. The physical design is reviewed in Section 3. The methods of producing and detecting the plasma compression are elaborated. Here, the experimental equipment is classified, illustrated and discussed in order to yield a comprehensive description of the project.

Section 4 lists the results which have been obtained, including x-ray and visible light spectra, visible light photographs along the axis of the source, and time-energy scintillator results which indicate the behavior of the radiation pulse as a function of plasma energy, system pressure and system preionization. Conclusions are presented in Section 5.

2. Theoretical Considerations

If a plasma is compressed and heated to temperatures such that kT is approximately 50 electron volts, it is possible to obtain a bremsstrahlung continuum of radiation in the wavelength range of approximately 20 to 1000 Angstroms. In addition, prominent line radiation will appear above the continuum depending on the gas used in the source and on the amounts and kinds of impurities present.

Three sources of radiation can be considered. When such a plasma is formed of a low Z gas such as hydrogen, all atoms are fully stripped. Most of the radiation then results from free-free electron interactions with the ions. The emitted bremsstrahlung spectrum is well known and has been used as a basis for design. At lower temperatures, recombination radiation (from free-bound electron interactions) is favored resulting in additional continuum radiation. Finally, small quantities of impurities of higher Z elements provide significant line radiation and also enhance continuum radiation.

Generally, it is sensible to evaluate details of the radiation semi-empirically, since many of the needed quantum mechanical and experimental quantities are not well known at the outset. Our approach involves a quantitative estimate of the bremsstrahlung radiation with the knowledge that recombination and excitation radiation may also contribute substantially. Only a qualitative estimate of these sources of radiation is formulated.

2.1. Bremsstrahlung Radiation

One of the important energy loss mechanisms in a very high temperature plasma such as a thermonuclear plasma is that arising from radiation. Radiant power approaching 10^6 watts is observed, for example, in the Scylla I plasma experiment (Ref. 1-4).

Deuterium ion temperatures approaching 1.3 kev have been obtained in Scylla, with electron temperatures of approximately 350 electron volts

reported by Jahoda (Ref. 5). In the latter reference the soft x-ray emission spectrum was observed by means of a single-crystal spectrometer in the wavelength range of 5 to 15 Angstroms which includes an emission peak at 10 Angstroms. In addition to the bremsstrahlung continuum, Jahoda also observes substantial recombination and excitation radiation from impurities. The latter are introduced as a result of plasma contact with the walls before the main compression.

We use the same plasma heating and compression technique as is used in Scylla but at much reduced energy since substantially lower electron temperatures are desired. The adaptation of this method is discussed in Section 3.

When monoenergetic electrons lose energy by free-free interactions, the bremsstrahlung radiation emitted is essentially flat per unit frequency interval up to a maximum (Ref. 6) given by E_e/h where E_e is the electron energy and h is Planck's constant. In a plasma, the electrons are usually distributed, at least approximately, according to a Maxwellian distribution. Then the total power radiated for a transparent plasma becomes: (Ref. 7).

$$P = 1.53 \times 10^{-25} Z^3 n^2 (kT_e)^{1/2} \quad \frac{ergs}{cm^3 sec} \tag{1}$$

where T_e is the electron temperature and kT_e is in electron volts, Z is the effective atomic number (or degree of ionization) and n is the electron density in electrons per cm^3. For the range of temperature, density and wavelength considered here, the absorption coefficient is always very small so that the above expression holds throughout.

The emitted spectrum is no longer flat, but varies approximately as $\exp(-h\nu/kT_e)$ in the case of a plasma. Expressed in terms of the power per unit wavelength interval the result is:

$$P_\lambda = \frac{1.90 \times 10^{-21} Z^3 n^2}{\lambda^2 (kT_e)^{1/2}} \exp\left(-\frac{1.24 \times 10^4}{\lambda\, kT_e}\right) \quad \frac{\text{ergs}}{\text{cm}^3 \text{ sec } \overset{\circ}{A}} \qquad (2)$$

where λ is in Angstroms.

It may be readily shown that the spectrum has a maximum located according to

$$\lambda_m (kT_e) = 6.2 \times 10^3 \, \overset{\circ}{A} \cdot \text{ev} \qquad (3)$$

Equation (1) has been used to compute the values shown in Table 1, for electron densities and temperatures spanning the range anticipated for the plasma source. For this purpose a value of $Z = 1$ has been chosen. While the power is given per unit volume, the result is numerically equal to the volume integrated power since a radiating volume of approximately one cm^3 is expected.

The table illustrates the insensitivity of the total radiant power to temperature. On the other hand, the strong dependence on electron density is in evidence.

TABLE 1

Bremsstrahlung Power Radiated from a Plasma for
Various Temperatures and Densities with Z = 1

KT_e \ n	10^{14}cm^{-3}	10^{15}	10^{16}	10^{17}
10 ev	4.75×10^3	4.75×10^5	4.75×10^7	4.75×10^9
50	1.08×10^4	1.08×10^6	1.08×10^8	1.08×10^{10}
100	1.53×10^4	1.53×10^6	1.53×10^8	1.53×10^{10}

(P in $\frac{\text{ergs}}{\text{cm}^3 \text{ sec}}$)

The source is estimated to result in electron densities of approximately 10^{16} cm^{-3}. Using this value and again taking $Z = 1$, the spectral power distribution is given by

$$P_\lambda = \frac{1.90 \times 10^{11}}{\lambda^2 (kT_e)^{1/2}} \quad \exp\left(-\frac{1.24 \times 10^4}{\lambda k T_e}\right) \quad \frac{\text{ergs}}{\text{cm}^3 \text{ sec } \overset{\text{o}}{\text{A}}}$$

Values of P_λ for various temperatures and wavelengths are tabulated in Table 2 using this expression. The last two columns in the table list λ_m as calculated from Equation (3) and the corresponding peak power P_m.

It may be seen from the table that there is considerable sensitivity of P_λ to temperature at the shorter wavelengths. Also, for the higher temperatures, there is a strong dependence on radiation wavelength. The source is expected to operate at a peak temperature of about 50 electron volts or more. It is seen from the table that the radiation per wavelength interval is more than an order of magnitude more intense in the 100 to 200 Angstrom range than that in the region of 1000 Angstroms for plasma at this temperature.

The information contained in Table 2 is illustrated graphically in Figures 1 and 2. In Figure 1, the spectral power density is plotted against wavelength for plasma electron temperatures of 20, 50, and 100 electron volts. These curves illustrate the enhancement of spectral content at shorter wavelengths for the higher plasma temperatures. The shift toward the shorter wavelengths of the spectral maximum and the narrowing of the spectrum distribution are also shown in the figure.

Figure 2 is a plot of the radiation intensity at several wavelengths as a function of the plasma temperature. It is demonstrated by the curves that the radiation at the longer wavelengths (500 to 1000 $\overset{\text{o}}{\text{A}}$) is essentially independent of the plasma temperature for temperatures

TABLE 2

Values of Spectral Power for Various Temperatures at Selected Wavelengths Between 50 and 1000 Angstroms

λ / kT_e	50 Å	100	200	300	500	1000	λ_m	P_m
10 ev	–	2.5×10^1	3.0×10^3	1.1×10^4	2.0×10^4	1.8×10^4	620	2.1×10^4
20	7.0×10^1	8.5×10^3	4.8×10^4	6.0×10^4	4.9×10^4	2.3×10^4	310	6.0×10^4
30	3.5×10^3	5.7×10^4	1.1×10^5	1.0×10^5	6.0×10^4	2.3×10^4	207	1.1×10^5
40	2.5×10^4	1.4×10^5	1.6×10^5	1.2×10^5	6.5×10^4	2.2×10^4	155	1.7×10^5
50	7.5×10^4	2.3×10^5	1.9×10^5	1.3×10^5	6.6×10^4	2.1×10^4	124	2.4×10^5
80	3.9×10^5	4.4×10^5	2.5×10^5	1.4×10^5	6.2×10^4	1.8×10^4	78	4.8×10^5
100	6.4×10^5	5.5×10^5	2.6×10^5	1.4×10^5	5.9×10^4	1.7×10^4	62	6.7×10^5

$$\left(P_\lambda \text{ in } \frac{\text{ergs}}{\text{cm}^3 \text{ sec Å}} \right)$$
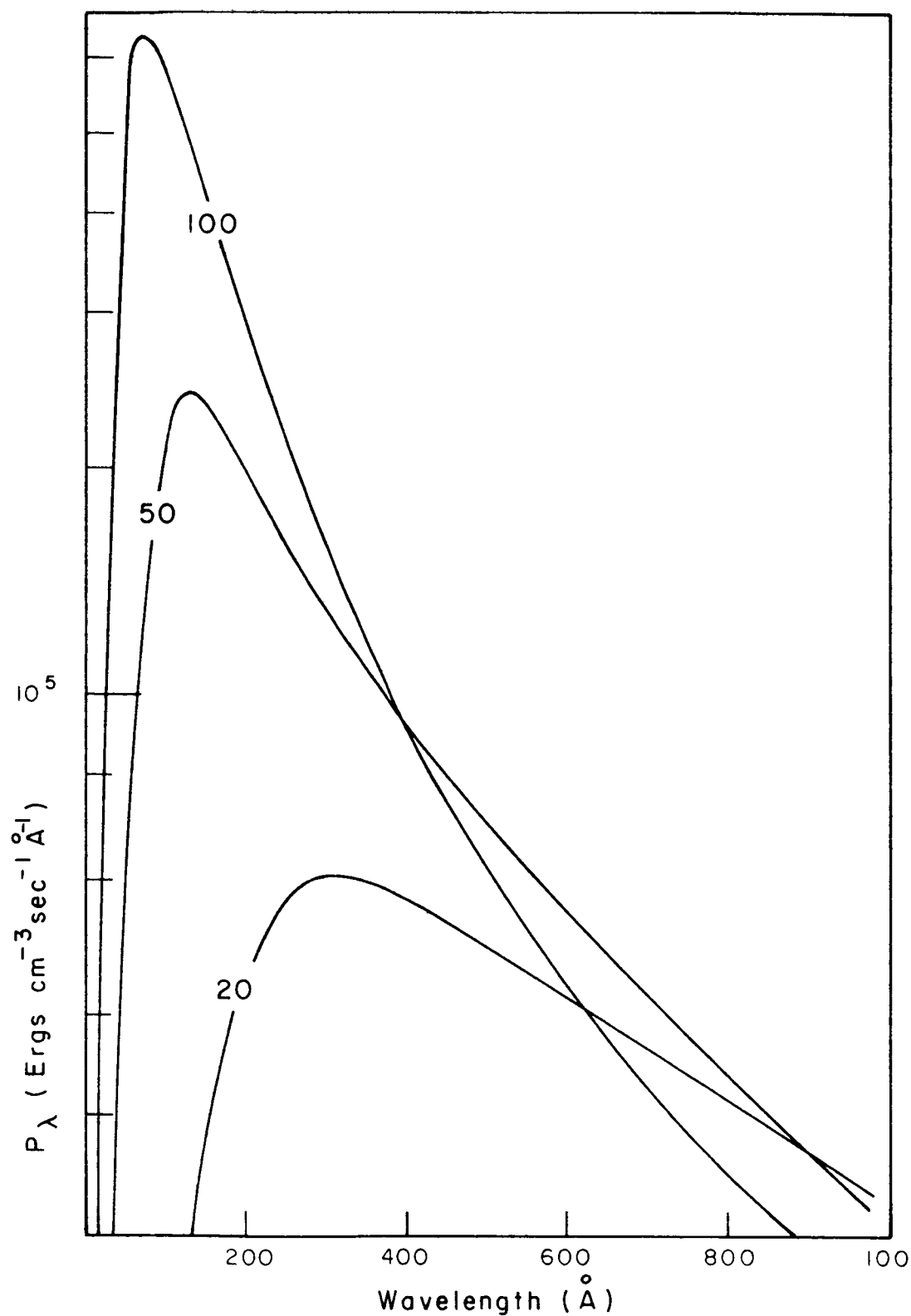
FIGURE 1.

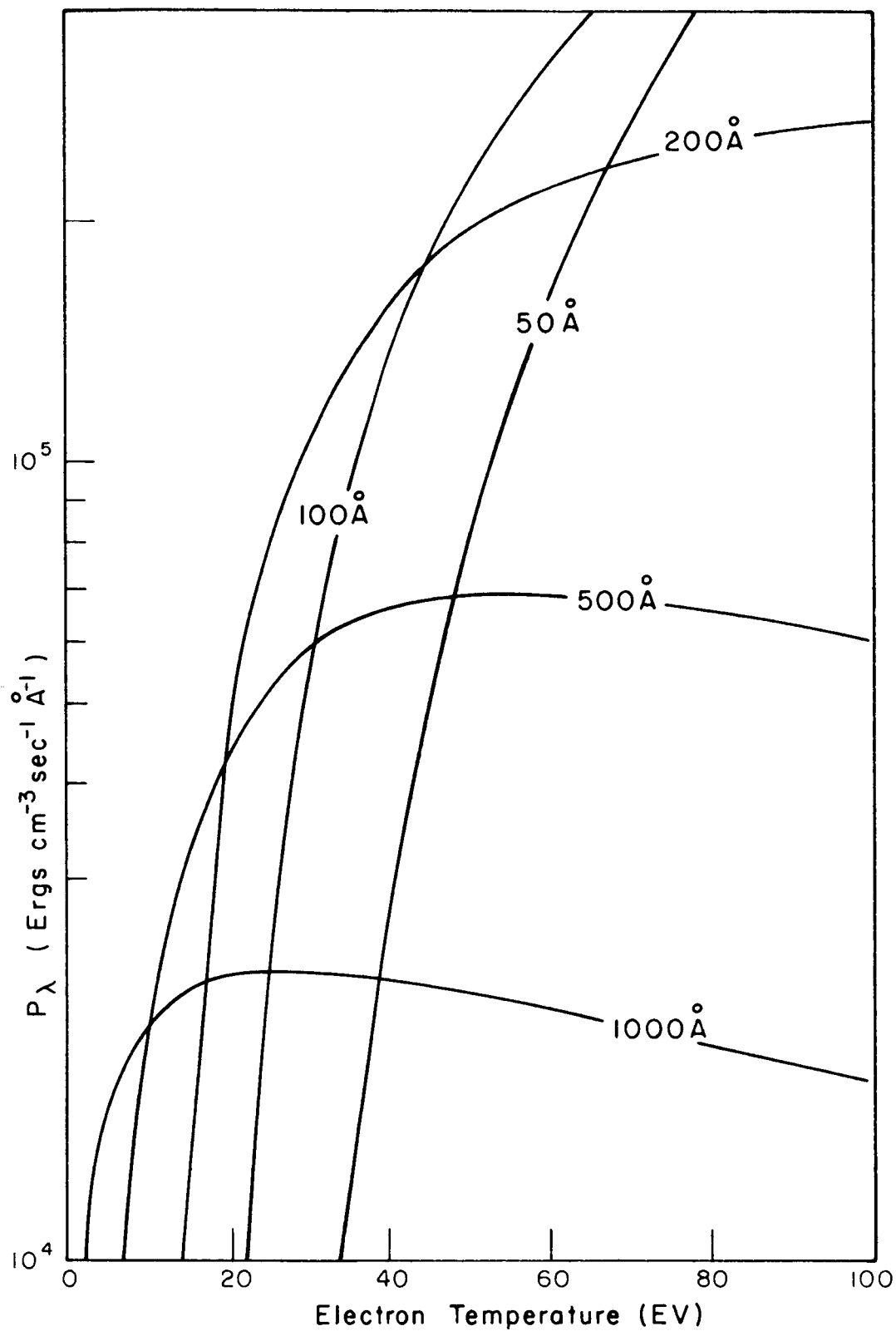BREMSSTRAHLUNG RADIATION SPECTRUM FOR
SEVERAL PLASMA TEMPERATURES.

91 - A1176

CE SCIENCES INCORPORATED

FIGURE 2.

BREMSSTRAHLUNG RADIATION AT SEVERAL WAVELENGTHS
vs. PLASMA TEMPERATURE.

91 - A1177

CE SCIENCES INCORPORATED

above about 20 electron volts. It is also seen that only slight gain
in intensity in the 100 to 200 Angstrom range is achieved for plasma
temperatures above about 50 electron volts. While the radiation
at 50 Angstroms is appreciable at temperatures of 50 electron volts,
a more marked gain in intensity is noted for higher temperatures.
For example, nearly an order of magnitude enhancement is achievable
at this wavelength by a two-fold increase in the plasma temperature.

In this section, some of the characteristics and quantitative esti-
mates of the bremsstrahlung radiation have been presented to illustrate
the workability of the source. In the following sections attention is
given to semi-quantitative considerations of the recombination and
excitation radiation which will also be present in the source.

2.2. Recombination Radiation

The free-bound electron reactions which take place in a plasma
lead to additional continuum radiation. In a low Z plasma at high
temperature, recombination is generally rare compared to the free-free
interactions giving rise to bremsstrahlung. This is due to the very
small cross section for recombination and its rapid decrease for
increasing electron energy. In hydrogen, for example, the recombination
cross-section for electron temperatures of 1 electron volt is only
2×10^{-21} cm^2 (Ref. 8) and is much smaller for temperatures of interest
in the compression source.

It is instructive to write the expressions for bremsstrahlung and
recombination radiation together following the presentation of Lukyanov
(Ref. 9). The spectral power densities for bremsstrahlung $P_{\nu b}$ and
recombination $P_{\nu r}$ in units of power per energy interval have the form:

$$P_{\nu b} = A\, n^2\, T_e^{-1/2} \qquad \exp \quad (-h\nu/kT_e)$$

(4)

$$P_{\nu r} = B\, (n^2/m^3)\, T_e^{-3/2} \quad \exp \quad -(h\nu - h\nu_i/kT_e)$$

where m is the principal quantum number of the level into which recombination occurs, $h\nu_i$ is the energy of the level and A and B are combinations of universal constants. The other quantities have been previously defined. The enhancement of bremsstrahlung relative to recombination radiation at high temperature is seen in Equation (4). On the other hand the electron density dependence is the same for both radiations.

Summing the radiation from both sources, one obtains:

$$P_\nu = n^2 T_e^{-1/2} \exp(-h\nu/KT_e) \left[A + B/m^3 T_e^{-1} \exp(h\nu_i/KT_e) \right] \qquad (5)$$

It may be seen that the combined radiation intensity has the same spectral distribution as the bremsstrahlung alone. Thus, recombination radiation simply increases the spectral intensity already described for bremsstrahlung in Section 2.1.

When elements of higher Z are present in the plasma, recombination radiation becomes increasingly important owing to the larger number of energy states into which recombination is possible and the general lowering of plasma temperature. In general, the second term in brackets in Equation (5) should be replaced by a summation over energy states. Jahoda's observations (Ref. 5) indicate substantial recombination radiation which adds to the bremsstrahlung continuum in Scylla. This arises largely from the impurities which are found in the Scylla discharge.

2.3. Line Radiation

For the plasma temperature range of interest in the radiation source, a pure hydrogen plasma will emit only a continuum since all atoms will be fully ionized. Actually, it is desirable to employ helium as the working gas to obtain the well known lines from this element for wavelength calibration purposes. Because of the relatively large

ionization potentials of helium (24.6 and 54.4 electron volts,) stripped atoms are rare at plasma temperatures in the region of 50 electron volts, while there is a high degree of single ionization.

In addition to radiation from helium, small amounts of impurities would contribute substantially to the line radiation. The additional impurity radiation is very useful in providing sufficient lines for wavelength calibration. Jahoda has observed impurity lines in Scylla from OVIII, NaX, MgXI and ALXII. These impurities are introduced by collision of the hot deuterium plasma with the ceramic walls of the discharge device. In addition to the line radiation, the presence of multiply ionized high Z elements in the discharge greatly increases the continuum radiation as may be seen from Equation (2).

The amounts and classification of the impurities which will be present in the source are not predictable from theory. However, it is expected that oxygen and carbon would be present. Table 3 is given to indicate some of the lines which are expected (Ref. 8). For each of the species the excited wavelengths, the excitation energy, ionization energies and total energy are tabulated. Only wavelengths below 1000 Angstroms are included. All energies are in electron volts.

At the 50 electron volts source temperature all of these lines can be excited. Apparently there exists a large concentration of O III and C III relative to the singly and triply ionized species. This is because a large fraction of plasma electrons possess more than sufficient energy for single and double ionization, but only a small fraction possess the required energy for triple ionization. Table 3 is only a partial tabulation of impurity lines which can be anticipated.

The prediction of line intensities is extremely difficult in practice. The theoretical line intensity is given by the proportionality

SCIENCES INCORPORATED

$$I \sim n_o \; \gamma^3 \; gf \quad \exp \; (-E/KT)$$

where n_o is the number densities of atoms in the ground state, g is the degeneracy of the upper energy state of the energy level E and f is the transition probability. Uncertainty in f-values and in n_o impose severe limitations in predicting results.

TABLE 3

Electron Energy to Excite Various States in

Oxygen and Carbon

Atomic Species	Wavelength	Excitation Energy	Ionization Energy	Total Ionization Energy	Total Energy
O II	834 A	14.58	13.61	13.61	28.46
O II	539	22.99	13.61	13.61	36.60
O III	835	14.88	35.15	48.76	63.64
O III	374	33.17	35.15	48.76	81.93
O IV	790	15.73	54.94	103.70	119.43
O IV	239	52.00	54.94	103.70	155.70
O II	858	14.44	11.26	11.26	25.70
O III	977	12.69	24.38	35.64	46.33

3. Physical Design

In order to create the compressed plasma, a capacitor is initially charged to a high potential, and is subsequently discharged rapidly through a single turn coil surrounding an insulating tube containing gas at a low pressure. The electromotive force associated with the rapidly rising current causes the gas to break down electrically and to become highly ionized. As the current rises to a maximum, the azimuthal electric field E_θ diminishes and a longitudinal magnetic field B_z increases to a maximum at the first quarter cycle. The rising magnetic field is partially excluded from the ionized gas and exerts an inward pressure on the plasma thereby compressing it to form a high temperature region near the axis of the coil. The compression is repeated at each maximum of the damped oscillatory current waveform typical of an RLC circuit.

3.1. The Production of X-Rays

3.1.1. The Capacitor Discharge Circuit

The basic discharge circuit is illustrated schematically in Figure 3. The capacitor C is charged through the charging resistor R to potential V_o. The discharge is activated by closing the switch S. A spark gap is used for this purpose. Current then flows through the parasitic circuit inductance L_1 (including the switch inductance) and resistance R_1 and through the single turn coil having the inductance L_2.

The storage capacitance and charging voltage have been selected to provide the desired values of E_θ and B_z for achieving the desired plasma compression and heating. The various circuit and performance parameters are tabulated in Table 4.

TABLE 4

Discharge Circuit and Performance Parameters

Compression Coil Inductance, L_2............ 4×10^{-8} henry

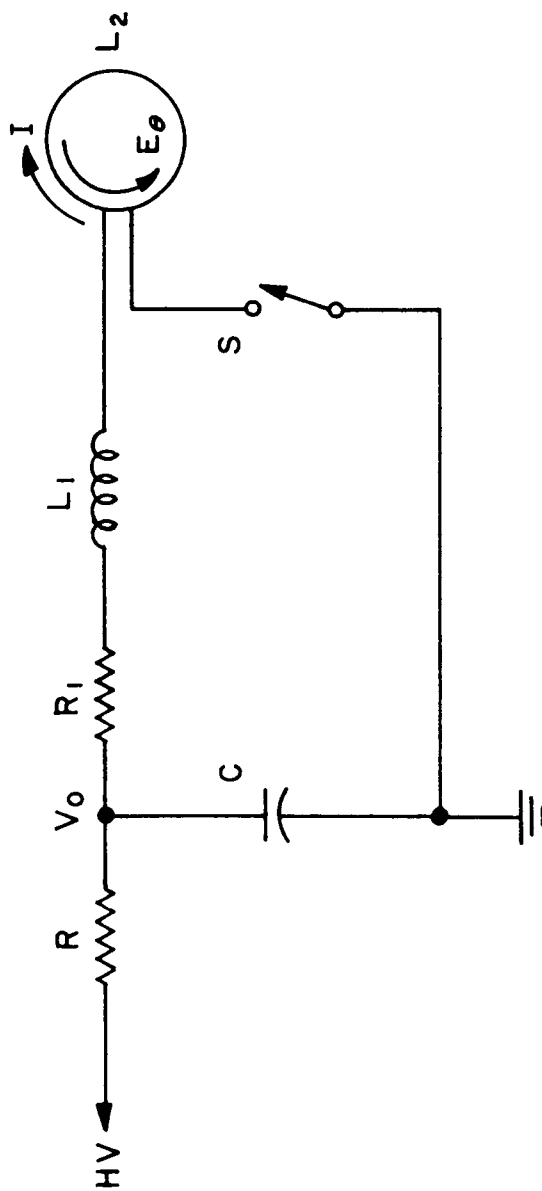External Circuit Inductance, L_1.............. 5×10^{-8} henry

SCIENCES INCORPORATED

FIGURE 3.

BASIC DISCHARGE CIRCUIT

TABLE 4 (cont.)

Charging Voltage, V_O .... 2.5×10^4 volts

Storage Capacitance, C .... 5×10^{-6} farad

Peak* Magnetic Field B_z .... 1.9×10^4 gauss

Stored Energy, $1/2\ CV_O^2$ .... 1.6×10^3 joules

Peak* Discharge Current, I_O .... 1.8×10^5 amperes

Peak* Azimuthal Electric Field, E_θ .... 900 volts cm^{-1}

Period of Oscillation, $2\pi\ (LC)^{1/2}$ .... 4.2×10^{-6} sec.

* These peak values correspond to the initial
or first quarter-cycle values. The exponen-
tial decay of the current and voltage wave-
forms leads to reduced values of I_O, B_z, and
E_0 at subsequent maxima. The decay is such
that the current pulse contains only three or
four significant maxima.

In achieving the parameters listed in Table 4, a spark gap is
mounted to the 25 KV, 5 µf capacitor in a coaxial housing yielding a
low inductance (4×10^{-8} henry) in the capacitor-spark gap portion of
the circuit. Special cables plug into the spark gap housing and thereby
connect the capacitor with the discharge coil. These cables (total 6)
are designed for low inductance, and contribute only 1×10^{-8} henry to
the total system. The discharge circuit is completed by the compression
coil which contributes an inductance of 4×10^{-8} henry. This system is
illustrated in Figure 4 and is described in greater detail in the following
subsections.

3.1.2. The Compression Coil

The coil has the form of a cylinder which is slightly deformed to
provide a magnetic mirror effect. This deformation has the result of com-
pressing the plasma toward a point near the geometric center of the

Spark Gap

Spark Gap Housing

Igniter Lead

Charging Lead

Cables To Compression Coil

Capacitor
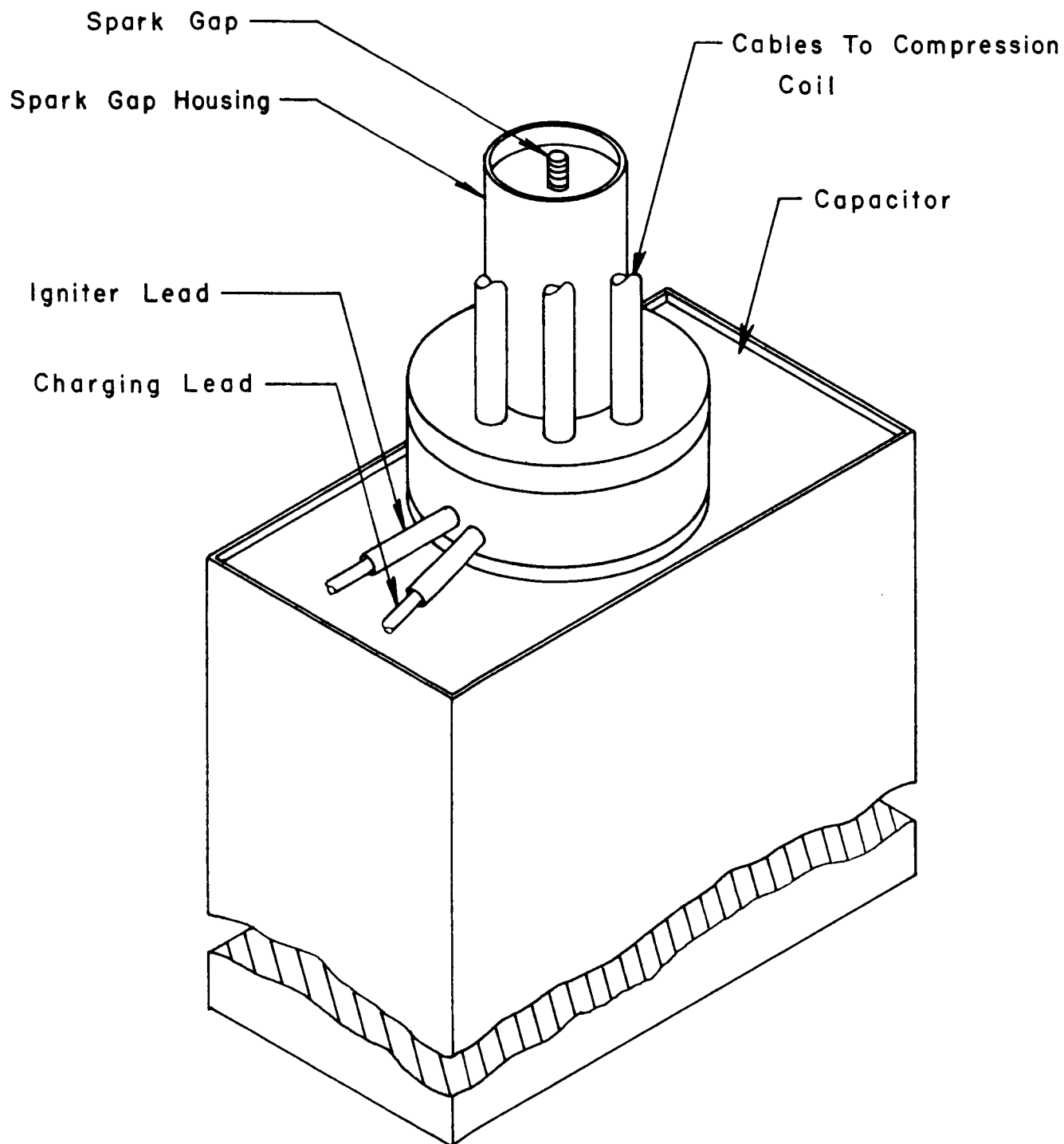
FIGURE 4.

DISCHARGE CIRCUIT LAYOUT

cylinder and provides for partial containment of the plasma near the current maximum. The geometry was optimized empirically in Scylla (Ref.1.) and provides excellent heating and compression of other plasmas as well. Therefore, the coil used in the Scylla device has been adopted directly in the present application. A sketch of the compression coil with indications of the important design dimensions is provided in Figure 5. The coil is shown in cross section in the figure and its relation to the pyrex discharge tube to be employed is indicated. The shape of the coil causes the magnetic flux to be somewhat concentrated at the ends of the coil as shown by the two field lines represented in the figure.

Figure 6 is an isometric sketch of the compression coil. The protrusion at the bottom of the coil is the mounting plate to which the six cables are connected. This coil has been machined from brass bar stock, and the portion of the assembly to which electrical connections are made is silver soldered to the compression coil. All sharp edges have been broken to reduce the tendency for electrical breakdown. As shown in Figure 4, this compression coil is connected through the cables to the spark gap which is described in the following section.

3.1.3. The Switching Mechanism

During the period of experimental work, two methods have been used for switching the high energy capacitor. In the initial stages, an ignitron tube, G.E. 7703, was used as the switch. However, this switch did not possess the required ruggedness to withstand continued service with high current pulses and slight mechanical vibrations. To arrange a less sensitive system, the ignitron has been replaced with a low inductance spark gap. This spark gap has been perfected, and far surpasses the ignitron for this purpose.
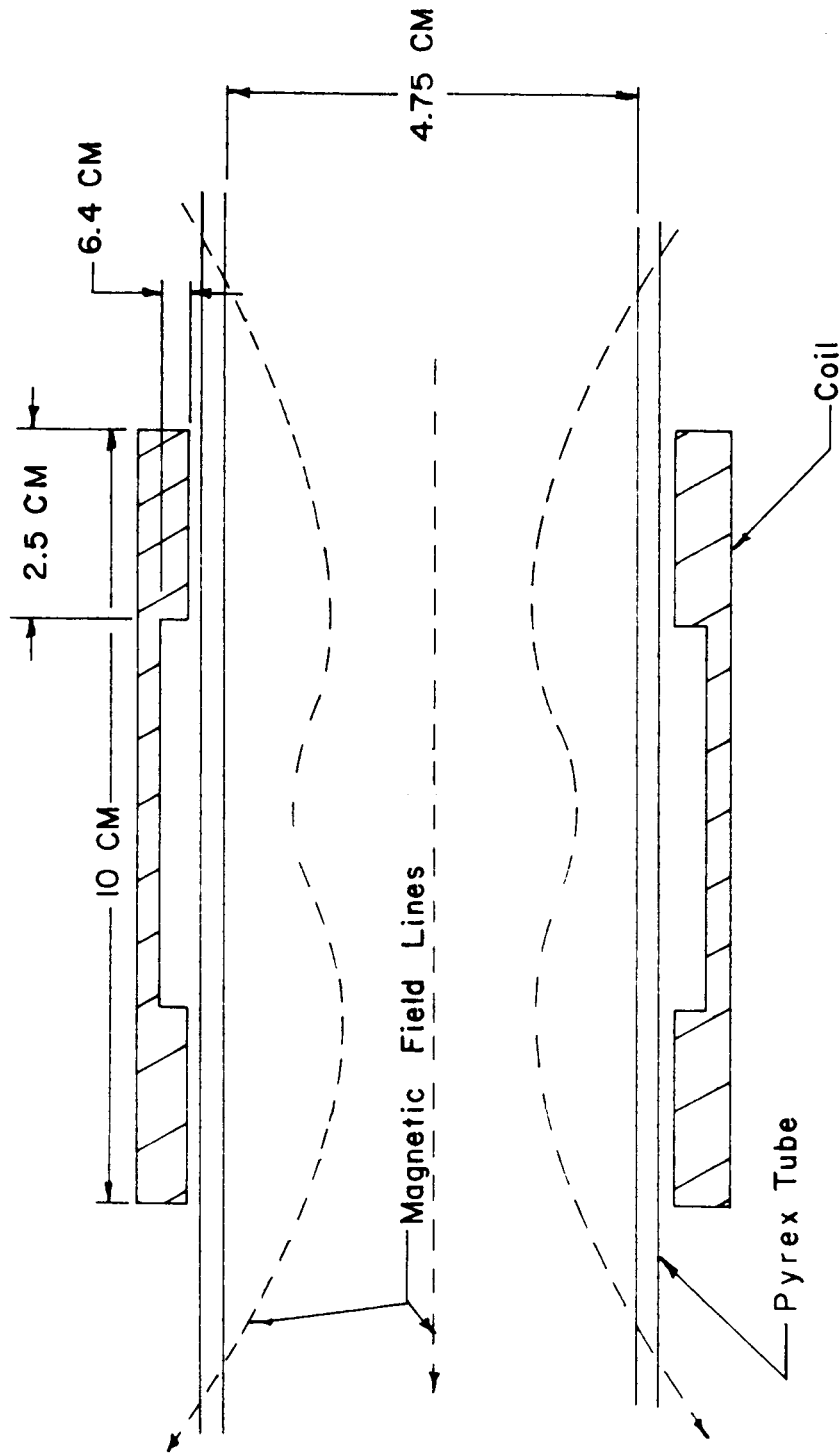
FIGURE 5.
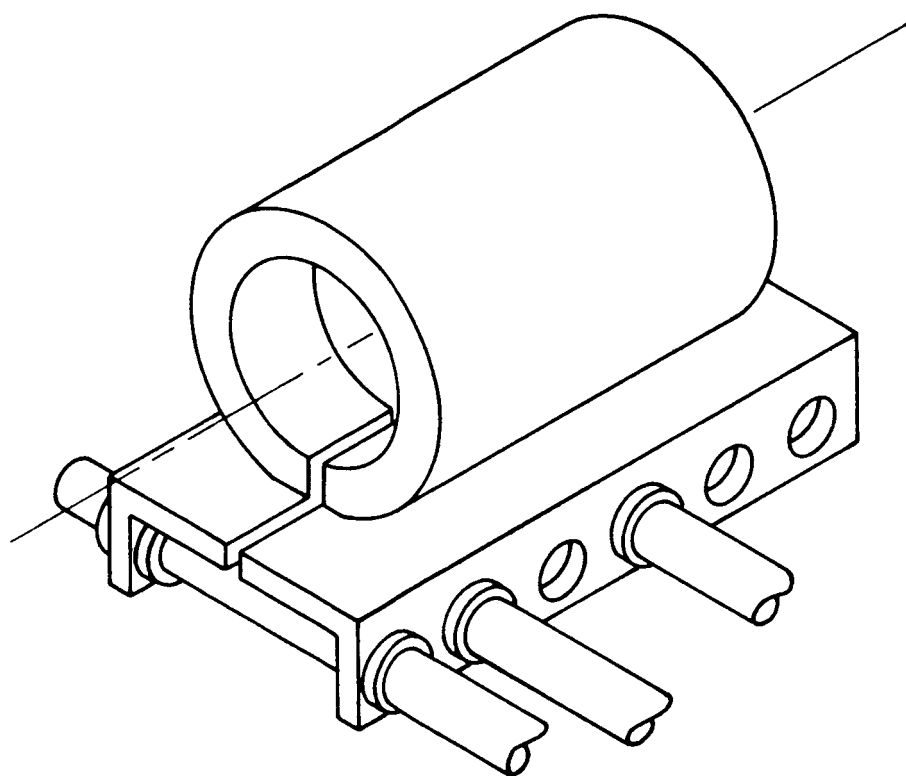
CROSS SECTION OF COMPRESSION COIL

FIGURE 6.

COMPRESSION COIL.

The spark gap is of nearly the same dimensions as the previously used ignitron and is incorporated in the same housing as the ignitron. It has approximately the same inductance but is more rugged and dependable. The gap is capable of over 1000 operations without attention. A schematic diagram of this gap is shown in Figure 7.

The design includes O-ring seals to prevent oil from entering the gap, and to allow disassembly should it become necessary for cleaning. The switch body is either ceramic or formica, the electrodes are stainless steel and the spark electrode is insulated from the cathode electrode by a glass-to-metal seal. All corners are rounded to limit Corona loss, and distances are adequate to eliminate spurious breakdowns at 20,000 volts. In operation, a high voltage pulse is applied between the trigger electrode and cathode. The trigger spark so formed then initiates the main capacitor discharge.

To fire the spark gap, the circuit shown in Figure 8 is employed. In operation, the gap is fired by closing switch S. By doing this, the grid of the 2D21 thyratron is pulsed. Conduction through the thyratron produces the trigger pulse on the output of the step-up high voltage pulse transformer. The secondary of the high voltage pulse transformer is connected to the cathode and trigger electrode as shown in Figure 8. The cathode is connected directly to the high voltage capacitor, and the capacitor charging supply.

3.1.4. The Capacitor Charging Supply

The high voltage capacitor charging supply utilizes a simple unfiltered bridge circuit to supply the voltage. This supply is designed to charge capacitors at a 20 ma rate to 20 KV in 10 seconds. A motorized output control is used for this purpose. In addition, a meter relay is used to preset the voltage to which the capacitor will charge.

These provisions allow the capacitor to be charged rapidly, and discharged as soon as the required voltage is reached. By doing this, the useful life of the capacitor is maximized, since the life of a capacitor is
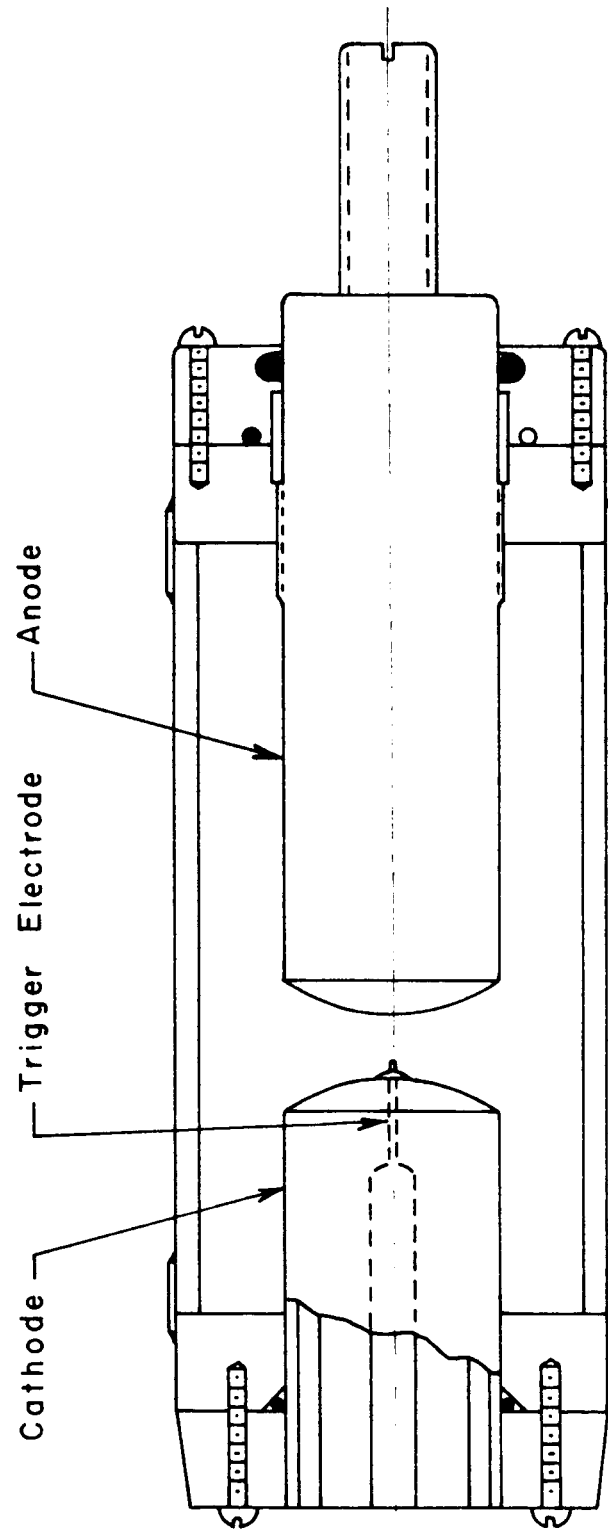
FIGURE 7.

THE SPARK GAP

Anode
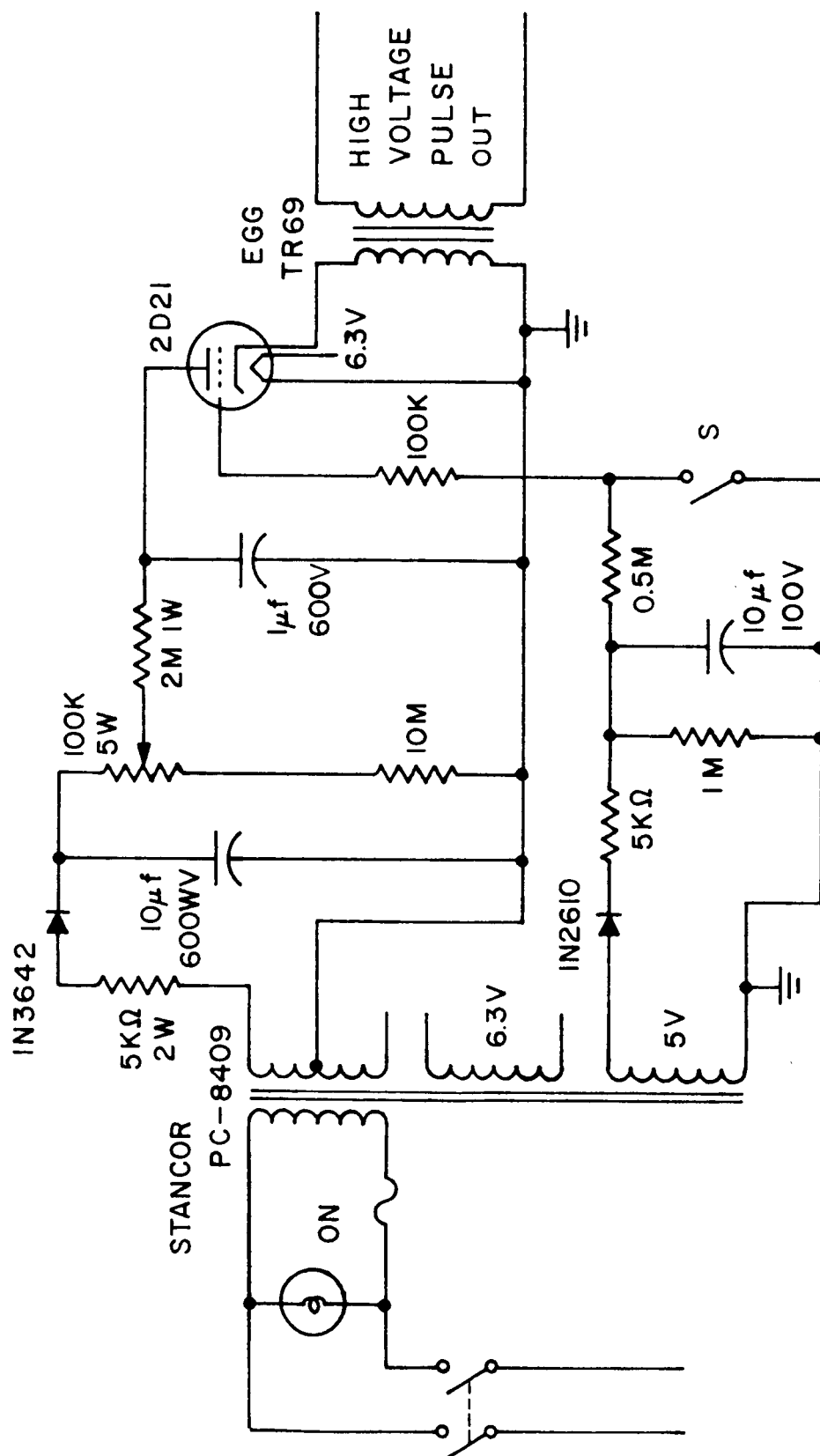
Trigger Electrode

Cathode

FIGURE 8.

SPARK GAP DRIVER CIRCUIT

determined by the time that the capacitor remains charged as well as by its discharge duty.

Once the capacitor is charged to the preset value, the high voltage turns off and the output control returns to zero (Fig. 9). This circuit is used in conjunction with an automatic cycling circuit which phases each of the operations required for the plasma pulse. That is, after the system charges to the preset voltage, a source of preionization is turned on, the spark gap switch is closed discharging the capacitor, the preionization is turned off, and finally a cooling delay is provided. In spite of the automation this circuit has been designed in such a way so as not to limit the manual control of the instrument in any way.

In the development work each of the aforementioned steps has been found necessary for an effective system. In fact, plasma compression will not occur without some preionization introduced into the system and the high voltage insulating materials will break down if they become overheated.

3.1.5. Preionization

Early in the experimental work it was noted that preionization is necessary in order to develop the compression pinch. As a result of this, several different methods have been tested. Among these the electrode free methods have proved most successful. Methods using electrodes contaminated the system so that they could not be recommended as a long term solution. Among the most successful procedures tested are ultraviolet, Tesla coil, and RF techniques.

The application of each of these to the system is quite direct. In the first case, a strong ultraviolet light source is held outside of the glass vacuum tube. In the second case, a Tesla coil is positioned beside the vacuum tube to produce ionization in the tube in the pressure range of $30\,\mu$ to $1700\,\mu$ He. In the third and most successful case, the RF antenna was wound around the outside of the glass vacuum tube close to the

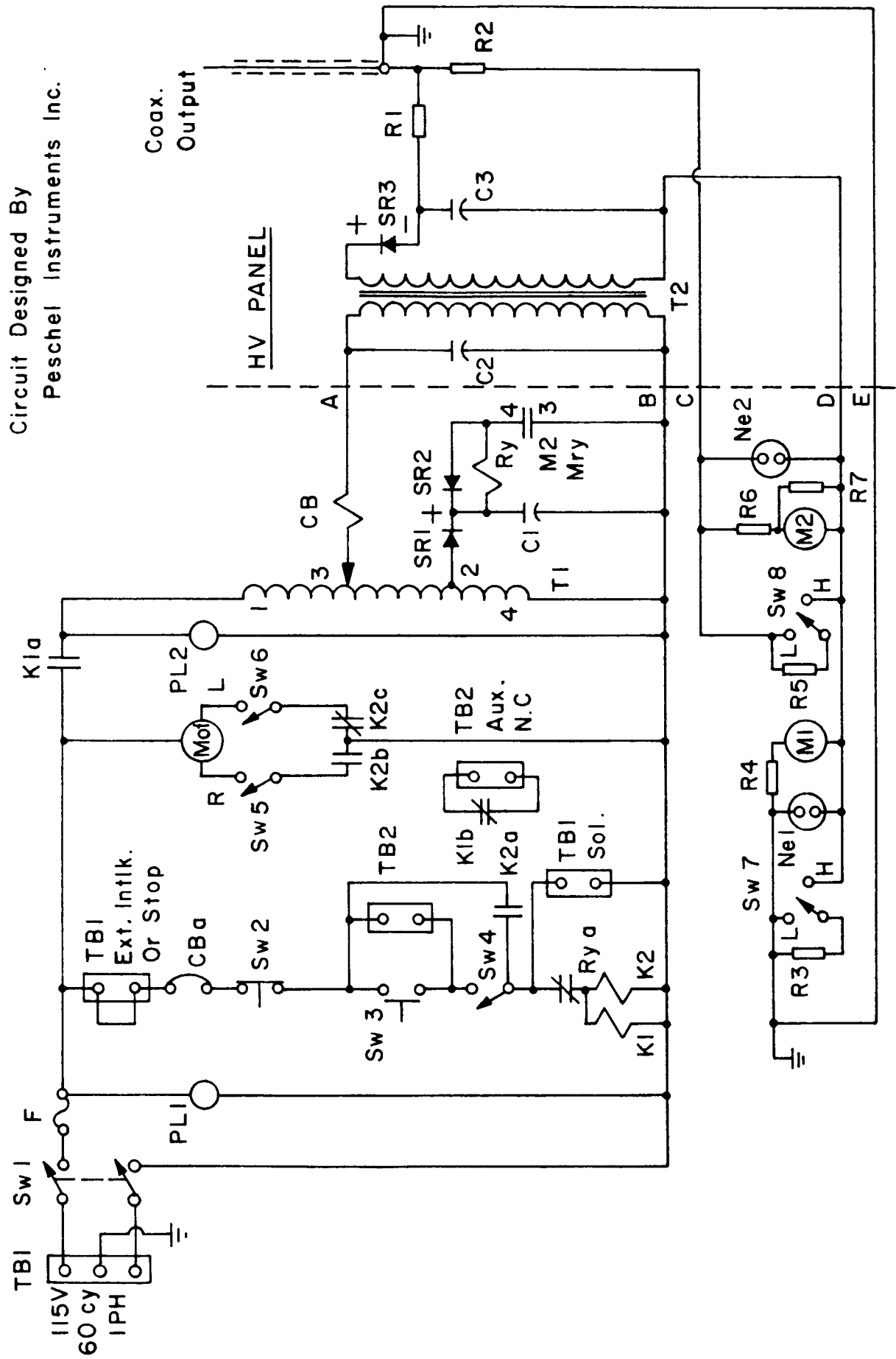Circuit Designed By
Peschel Instruments Inc.

FIGURE 9.

HIGH VOLTAGE POWER SUPPLY CIRCUIT

91-A2257

ACE SCIENCES INCORPORATED

discharge coil. With this system, a commercially available RF generator is used in conjunction with an RF transformer to improve the coupling between the generator and the vacuum tube.

In Section 4, data are presented to show that the RF system of preionization is the most effective system which has been evaluated.

3.1.6. The Vacuum System

As indicated in Section 2, the discharge system requires a partial vacuum in order to operate satisfactorily. The experimental requirements have been fufilled by the system shown in Figure 10. This system includes a mechanical pump, a glass vacuum trap filled with Zeolite to retard the backstreaming of oil from the mechanical pump, a thermocouple gauge for monitoring the pressure and an inlet valve for injecting gas into the vacuum system. This system has operated satisfactorily for all the experimental requirements, having been used in the pressure range between 10 to 1700 microns.

A second system has been designed for the final instrument to meet the need for a 10^{-6} torr vacuum at the slit entrance of the Goddard Spectrometer. In order to attain 10^{-6} torr, differential pumping is used at the junction between the discharge tube and the spectrometer slit. This new pumping system is shown in Figure 11. The remainder of the pumping system is similar to that illustrated in Figure 10. However, the mechanical pump used to rough pump the system does not pump through the differential slit restriction. Once the system has been pumped into a region sufficient for the diffusion pump, the mechanical pump is valved off and all pumping is then done through the differentially pumped region.

The most effective differential pumping arranagement found is a set of thin diaphragms, spaced along a 12 cm path, each cut with an opening to allow 1° acceptance angle, and in each, the area of the opening is much less than the area of the diaphragm. Under

RADIATION ANALYZING SECTION

Compression Coil

Brass Vacuum Flange

Microvalve

Helium Inlet

Zeolite Trap

TC Gauge

Bench Top

Spark Gap

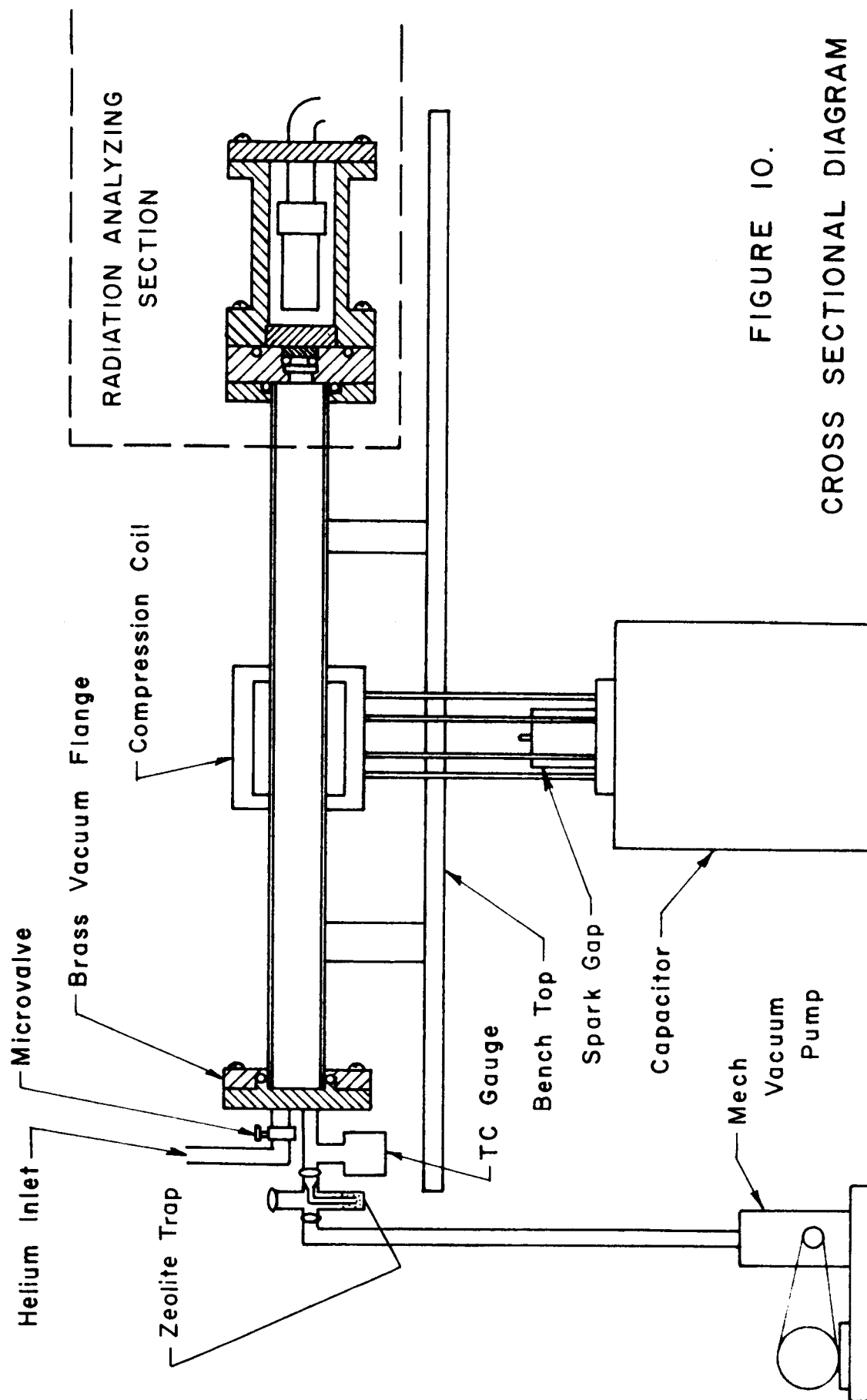Capacitor

Mech Vacuum Pump

FIGURE 10.
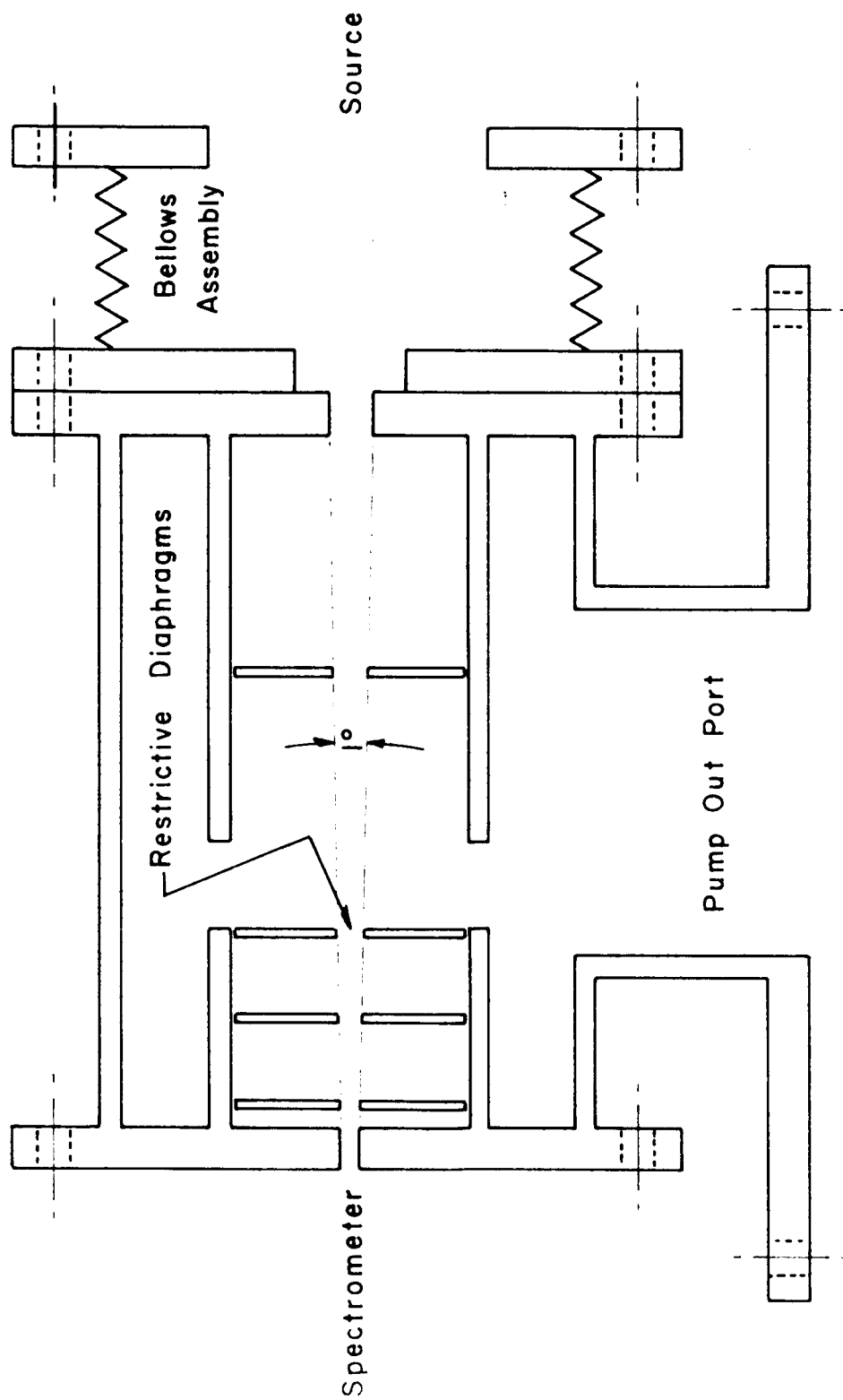
CROSS SECTIONAL DIAGRAM

OF MECHANICAL HARDWARE

FIGURE II.

DIFFERENTIAL PUMPING ARRANGEMENT

these conditions, the equation for calculating the conductance of a
slit is given by Equation 6 (Ref. 10)

$$C = \frac{k\,T}{2 - M}\,A \qquad\qquad (6)$$

where A is the slit area, k is the Boltzmann constant, T the gas
temperature in degrees Kelvin and M the mass of the gas molecule
involved.

Substituting the following values into Equation (1)

$$k \;=\; 1.35 \times 10^{-16}\ \text{erg/degree}$$
$$T \;=\; 300^{\circ}K$$
$$M \;=\; 4\,(1.7 \times 10^{-24})$$

the conductance for several slit restrictions can be determined, and
the conductance for each set of slits can be determined and is indi-
cated in the pumping schematic illustrated in Figure 12.

The quantity of gas (Q= CP) pumped with the spectrometer's pumps
must be equal to the quantity admitted through C_2. Therefore $Q_{out} =$
$Q_2 = 2.75 \times 10^{-3}$ mm^2/sec. It follows that P_D must be less than
7×10^{-3} mm Hg. The quantity of gas Q_1 flowing into the differentially
pumped chamber is 2.5×10^{-1} mml/sec and the required pumpong speed
for the differently pumped chamber is 36 l/sec. Assuming 2/3 loss in
pumping effeciency from the baffles and valves, the differential pumps
must have a speed in excess of 110 l/sec. Considering the Mercury
Diffusion Pumps, the CVC pump, MHG-50, would be adequate and a
port for this size pump is included in our design.

The differential slit arrangement mates with the front flange of the
x-ray spectrometer and the other side mates with a bellows used to elimin-
ate mechanical stress. The bellows in turn mates with the plasma com-
pression tube. In our design, the slits are all prealigned and perman-
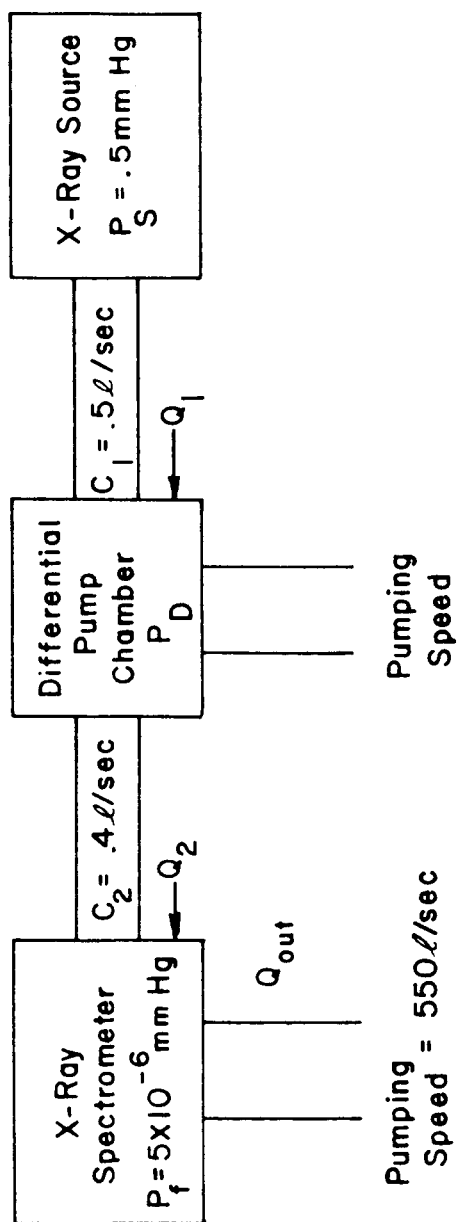ently locked in position. The only adjustment which needs to be made is

FIGURE 12.

DIFFERENTIAL PUMPING SCHEMATIC

alignment of the differential pumping restriction with the spectrometer slit.

3.2. The Analytical Techniques

Two methods have been used to obtain quantitative and qualitative evaluation of the x-ray pulse from the plasma compression instrument. A quantitative measure of the pulse magnitude has been obtained from a photomultiplier coated scintillator arrangement. The qualitative results have been obtained from a small vacuum spectrometer located at the end of the plasma compression tube. In the following subsections, each of these analytical methods is discussed. Results are described in Section 4.

3.2.1. The Photomultiplier-Scintillator Technique

For the quantitative stages of the analysis of the optical properties of the source, the assembly shown in Figure 13 has been used. This assembly utilizes a photomultiplier-fluor detector scheme. The scintillator material converts x-rays to visible light which then pass out of the vacuum system and are detected by the photomultiplier tube.

Pilot B has been chosen as the fluorescent material, and it has been coated by Pilot Chemicals Inc. with 2000 $\overset{O}{A}$ of aluminum film to make it opaque to visible light. A small diaphragm in front of this scintillator is used to limit the x-ray exposure. In some experiments, a magnetically operated glass shutter has been used over this diaphragm in order to certify the opacity of the Aluminum film. A glass plate is used on the far side of the scintillator as a transparent vacuum barrier between the fluorescent material inside the vacuum system, and the photomultiplier tube outside the vacuum system. The photomultiplier selected for detecting the scintillations is an RCA type, number 6199. Mu metal supports the photomultiplier in its correct position in contact with the glass plate and shields the photomultiplier from stray magnetic fields. The preamplifier circuit is housed with the photomultiplier tube. This circuit is illustrated in Figure 14.
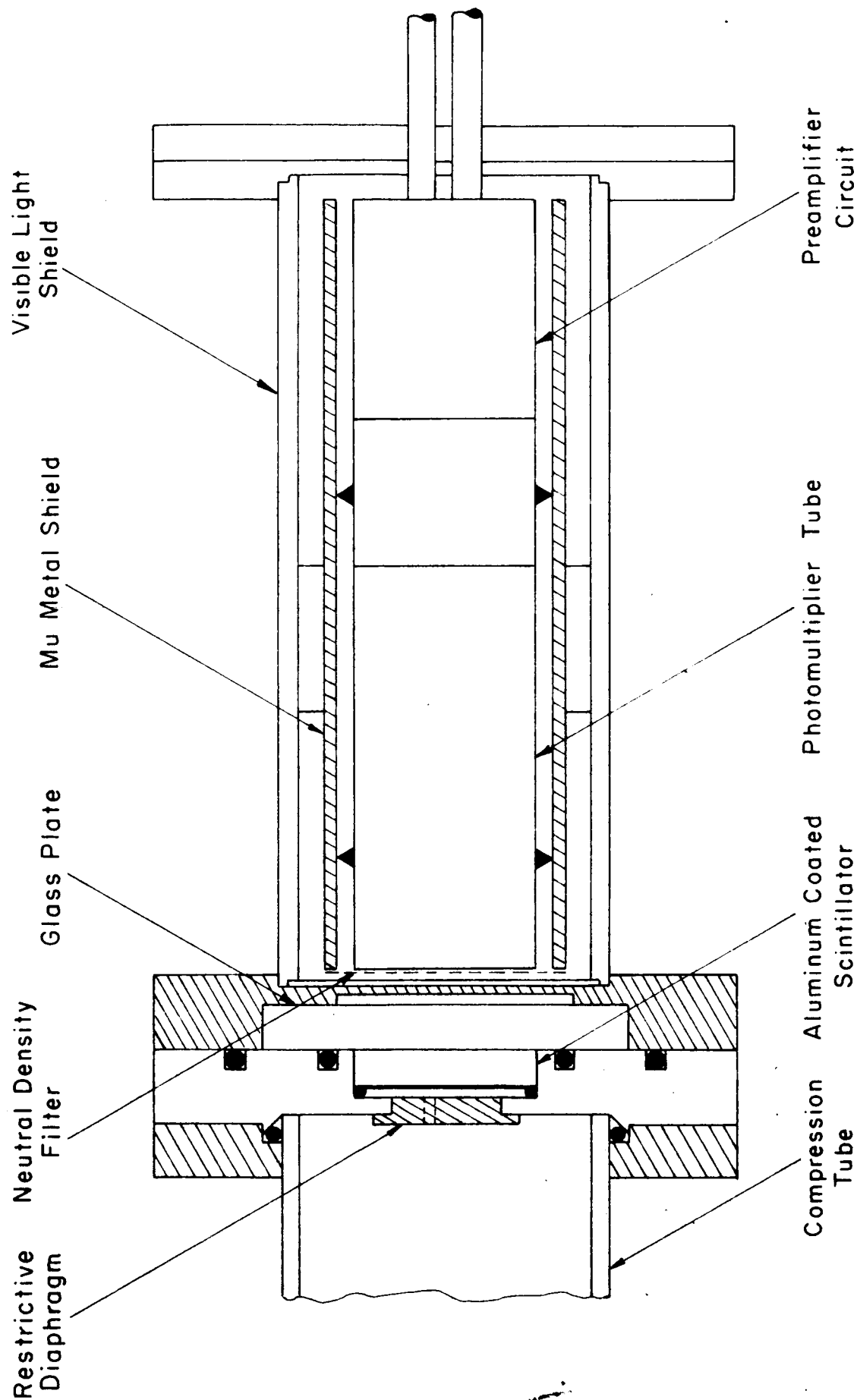
Visible Light Shield

Preamplifier Circuit

Mu Metal Shield

Photomultiplier Tube

Glass Plate

Neutral Density Filter

Aluminum Coated Scintillator

Restrictive Diaphragm

Compression Tube

FIGURE 13.

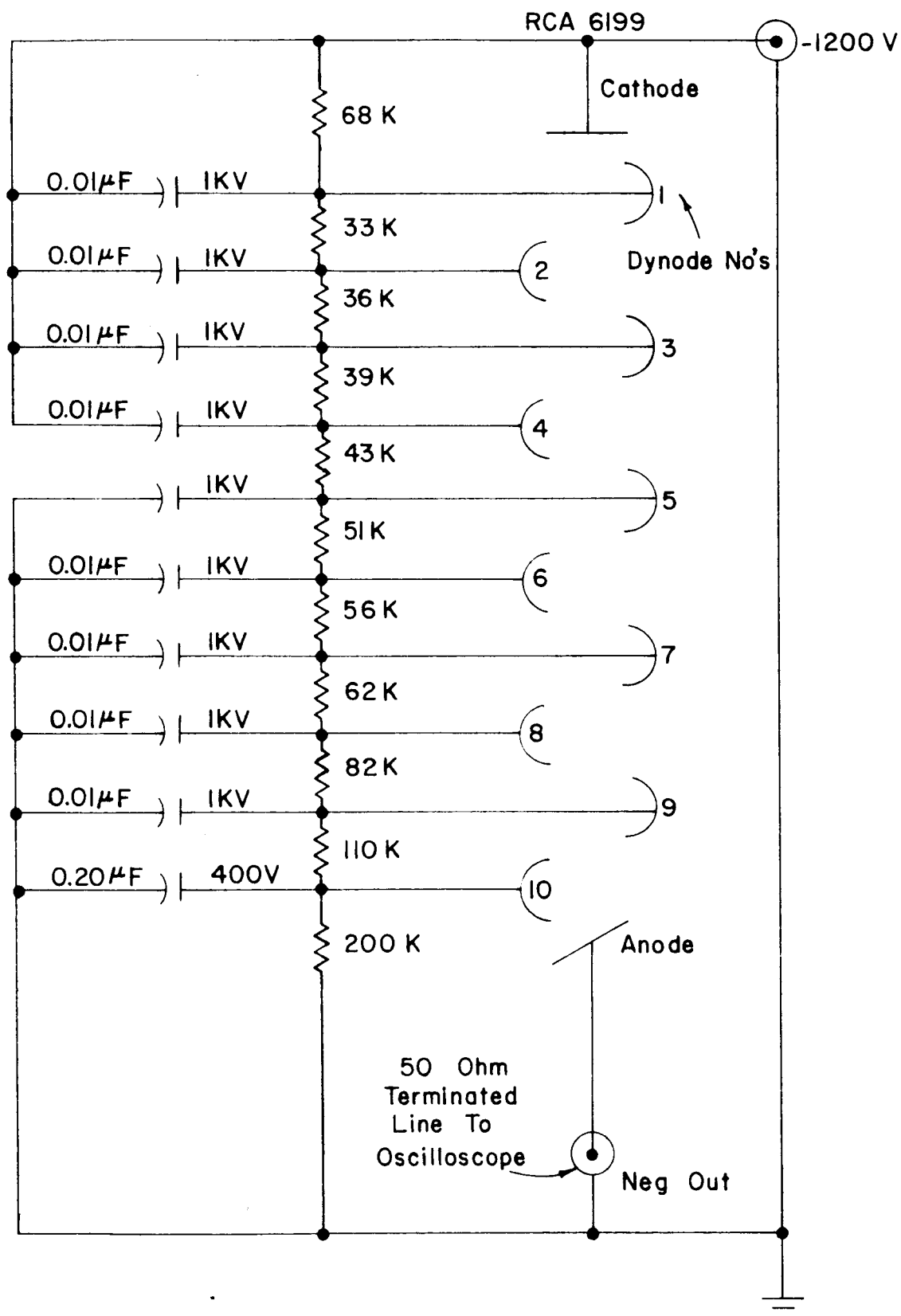PHOTOMULTIPLIER – SCINTILLATOR ARRANGEMENT.

ACE SCIENCES INCORPORATED

FIGURE 14.

PHOTOMULTIPLIER DETECTION CIRCUIT

This circuit has been selected because it is specially suited
for measuring light intensity vs. time. With the anode driving a
50, 100 or 200 ohm terminated line, it has a frequency response of
at least 100 mc, the limit being set by the transit time spread of
electrons through the multiplier which will be of the order of 4 or 5
nanoseconds. This circuit will deliver about 40 ma for at least one
microsecond with reasonable linearity up to 30 ma. The voltage source
used with the preamplifier is commercially available from the John
Fluke Manufacturing Co.

3.2.2. Spectroscopy

In order to investigate the dispersed vacuum ultraviolet and
soft x-ray nature of the pulse, a one meter grazing incidence
vacuum spectrograph was installed in a small vacuum chamber and
an optical baffle was built to limit the light reaching the spectrograph.
The instrumentation was arranged so that the spectrograph's vacuum
chamber lined up and coupled with one end of the Pyrex compression tube.
This assembly is shown in Figure 15. In this diagram the interrelation-
ship between the spectrograph, its vacuum chamber, and the optical
baffle connection between the compression tube and the vacuum
spectrograph are shown. The spectrograph vacuum chamber was pro-
vided with sliding racks so that the spectrograph could be entirely
removed from the vacuum system while loading the SWR film.

The vacuum chamber was pumped around the spectrograph slit.
This pump-out port also served as an optical baffle to eliminate
scattered light in the system. The optical baffle was adjusted so
that the light reaching the spectrograph grating was limited, while
providing adequate pumping . With this design, the spectrograph was
at the same pressure as the source, which, during the most successful
tests, was about 100 microns. A bellows assembly was used so that
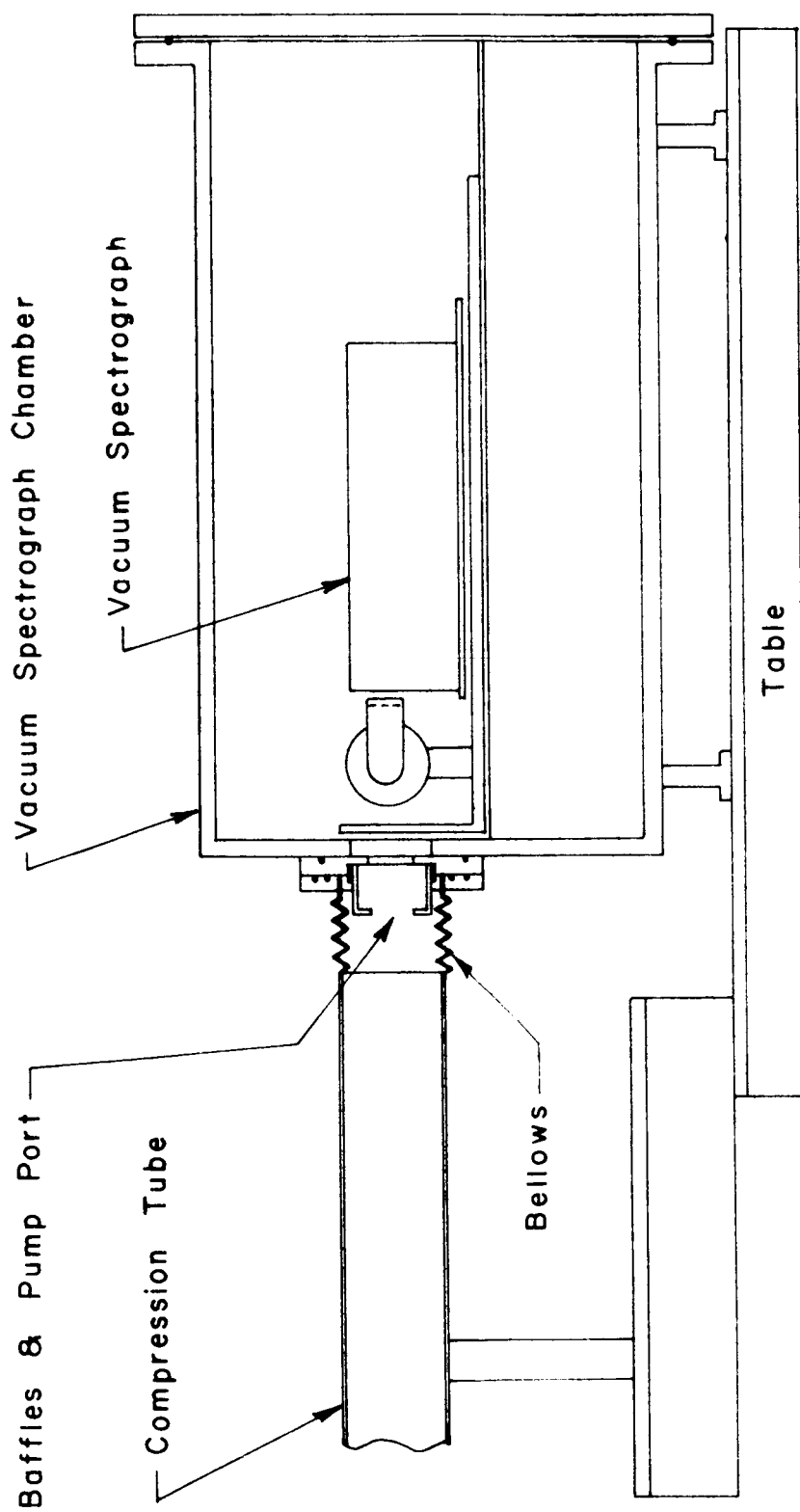the axis of the compression tube could be aligned with the axis of the

FIGURE 15.

VACUUM SPECTROGRAPH ASSEMBLY.

vacuum spectrometer without breaking the vacuum connection between the two.

The connections for the visible light spectrometer were simpler since the visible light spectrometer does not require a vacuum for successful operation. In this case, the glass compression tube was closed off with a glass plate, and our 1.5 meter Wadsworth Grating Spectrograph was moved onto the axis of the plasma compression tube.

Our research results have showed that the alignment of the vacuum spectrometer is critical. In fact, misalignment has been the most troublesome problem in the development project. Both the alignment and the maintaining of the alignment have contributed to the problem. For this reason, it is necessary to provide adequate methods for alignment of the instrumentation.

Recently, Kolb and McWhirter (Ref. 11) have studied the ionization rates and power loss from θ-pinches by impurity radiation. They have shown that the radiation from different impurities has originated from different parts of the discharge tube depending on the impurity. They also slow that different impurities radiate with different time histories.

For these reasons, the final instrument is being prepared with a fine vernier control in order to adjust 5 degrees of freedom independently. This will permit adjustment of the source position for maximum performance, and for evaluation of impurity distributions.

4. Results

Diagnostic results have been collected with two objectives:
(1) to establish final operational parameters, and (2) to ascertain
the radiative nature of the plasma compression. Consequently, three
types of measurement have been made. These include visible light
measurements, x-ray pulse shape measurements, and x-ray spectral
measurements. Visible light measurements have included visible spec-
troscopy, visible light pulse shapes and photographs of the plasma com-
pression. X-ray pulse shape data have been used for examining the
shape of the x-ray pulse as a function of pressure, and as an indication
of the reliability of the instrumentation. Finally, x-ray spectra have
been used to reconfirm the performance of the source, and to partially
establish the distribution of radiant power.

4.1. Visible Light Measurements

Figure 16 shows typical visible light spectra. The emission
spectrum shown here has been measured with a 1.5 Meter Wadsworth
Grating Spectrograph. As expected, these results show a predominance
of lines from both neutral and singly ionized helium. A few of these
are labelled in the figure. The five spectra shown in this figure were
all taken at the same pressure (1 mm Hg) and slit width (100 microns).
The film used was Tri-X and the spectrograph had a speed of f-32, and
a dispersion of approximately 11 A°/mm. Each spectra was obtained by
exposure to five capacitor discharges. The five different spectra were
taken at different capacitor voltages, from 15 to 19 KV inclusive. The
lines are only slightly more intense at the higher voltages.

Time integrated photographs were taken of the actual plasma
compression. The purpose of this was to measure the region of maximum
radiation and to verify visually that a pinch actually exists. Figure 17
is a picture along the axis of the compression tube. This picture was
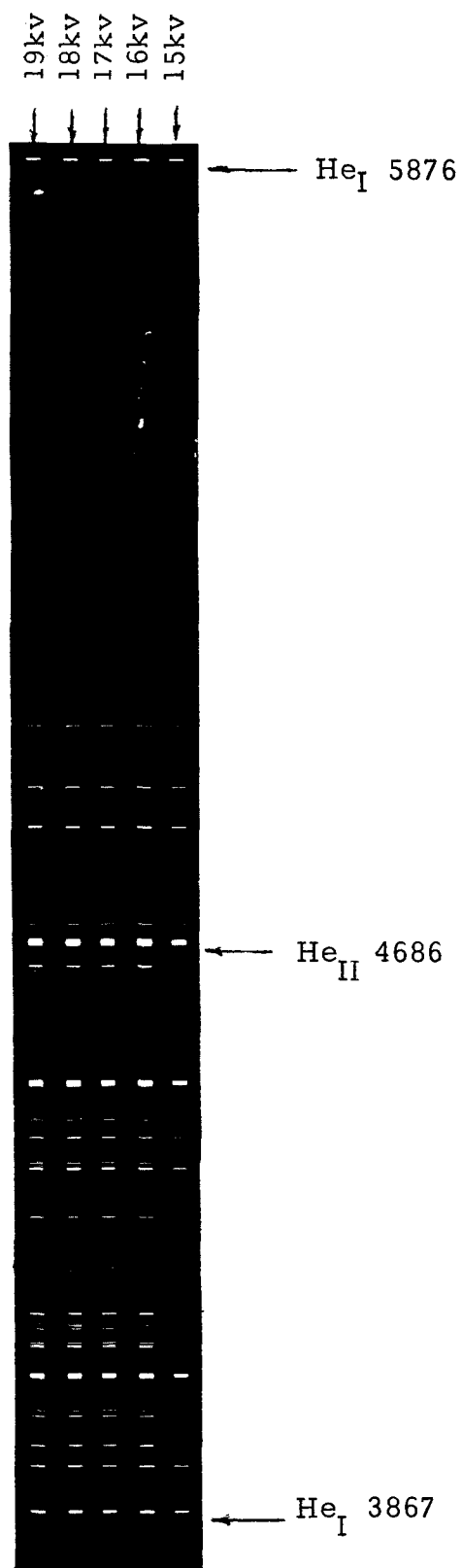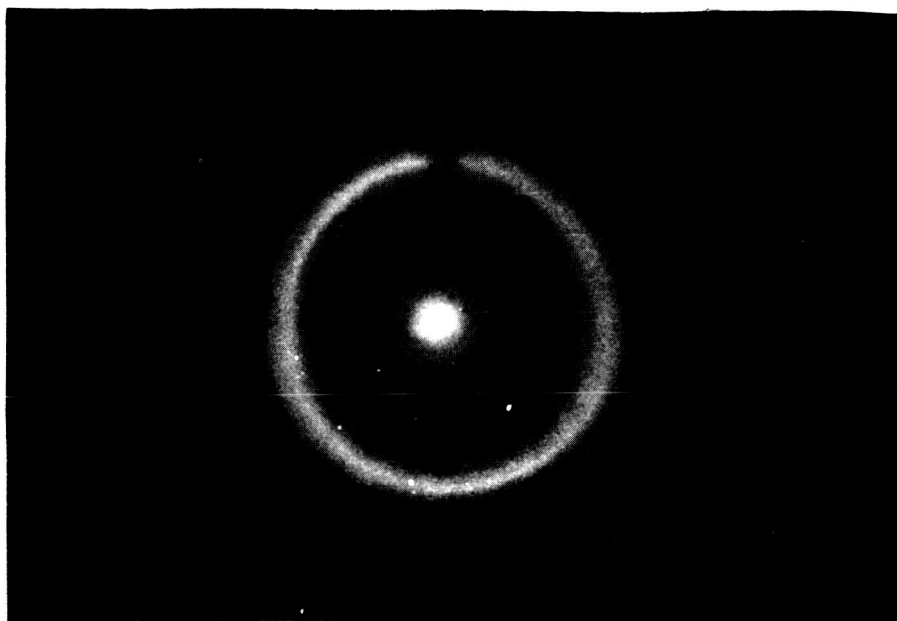taken with the photomultiplier scintillator assembly removed, and the

SCIENCES INCORPORATED

Fig. 16. VISIBLE SPECTRUM

FROM THE PLASMA COMPRESSION

Pressure: 1 mm Hg.

Lens Opening: f 16

Attenuation: 10^3

Film: Tri-X

Fig.17. PICTURE ALONG THE AXIS
OF THE PLASMA COMPRESSION

camera focussed at the center of the discharge coil. However, the depth of field was great enough so the whole tube was in focus. This picture was taken with Tri-X film, a lens opening of f-16 and a neutral density filter of 10^3 times. The presence of the plasma compression is evidenced by a bright spot at the center of the photograph, diminishing as the distance from the center increases. In the picture, the concentric rings of high intensity are reflections from the compression tube itself. The area of maximum pinch has been estimated to have a diameter of less than 0.5 inches, a result consistent with predicted values.

Other visible measurements incorporated the photomultiplier to make time-energy analysis. To make these measurements, the aluminum coated scintillator was removed from in front of the photomultiplier, and neutral density filters were installed in its place. These results are shown in Figure 18. By comparing a and b it is obvious that higher light intensities are available at higher pressures and the pulses occur during earlier cycles of the ringing discharge at the higher pressures. Trace c shows the long term characteristics of the emitted light. This was obtained by attenuating the signal (10^5 times),and by using a slow scan speed as indicated in the figure.

4.2. X-Ray Pulse Shape Measurements

Results obtained with the scintillator photomultiplier apparatus are shown in Figure 19 and 20. Figure 19 shows the x-ray pulses as a function of system pressure. It is seen that the pulse size is maximum at a higher pressure, and the pulses occur later in time at lower pressures. In this experiment, the discharge voltage was 15 KV, and the only parameter changed was the system pressure.

The pulse shape seen here is a series of pulses, each pulse occuring near the maximum of the LRC current cycles. In this figure, it is also apparent that the pulse length is approximately $4\mu s$, a

(a) 2 v/cm ↑

Pressure: 1200 Microns

2 μs/cm ⟶

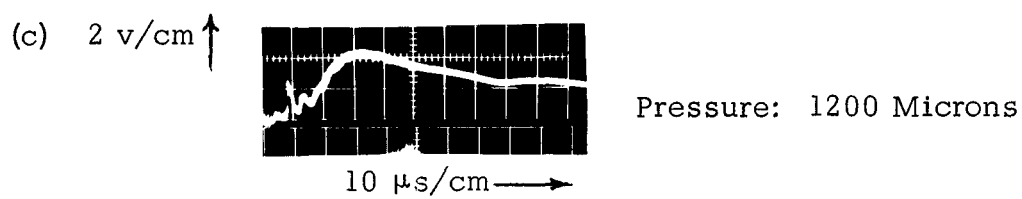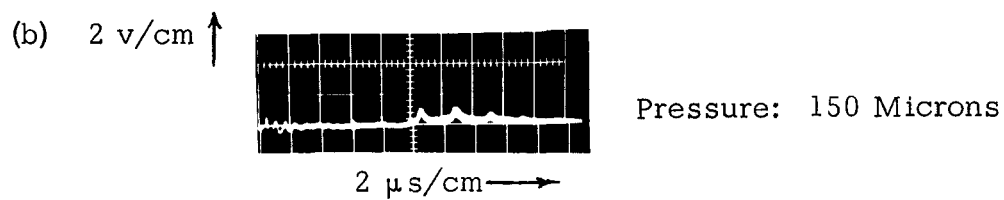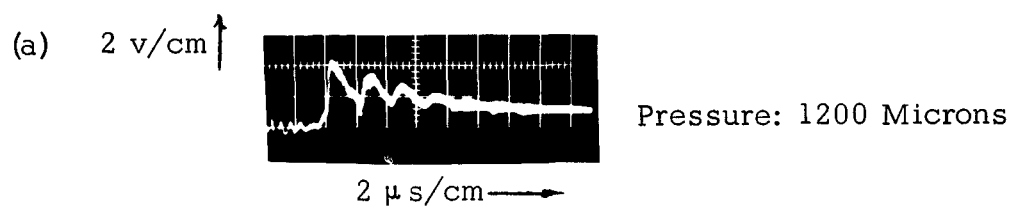(b) 2 v/cm ↑

Pressure: 150 Microns

2 μs/cm ⟶

(c) 2 v/cm ↑

Pressure: 1200 Microns

10 μs/cm ⟶

Fig.18. VISIBLE LIGHT PULSE SHAPE vs TIME

(a) 5 v/cm ↑   Pressure: 1500 Microns He

2 μs/cm——→

(b) 5 v/cm ↑   Pressure: 1200 Microns He

2 μs/cm——→

(c) 5 v/cm ↑   Pressure: 800 Microns He

2 μs/cm——→

(d) 5 v/cm ↑   Pressure: 80 Microns He

2 μs/cm——→

(e) 5 v/cm ↑   Pressure: 60 Microns He

2 μs/cm——→
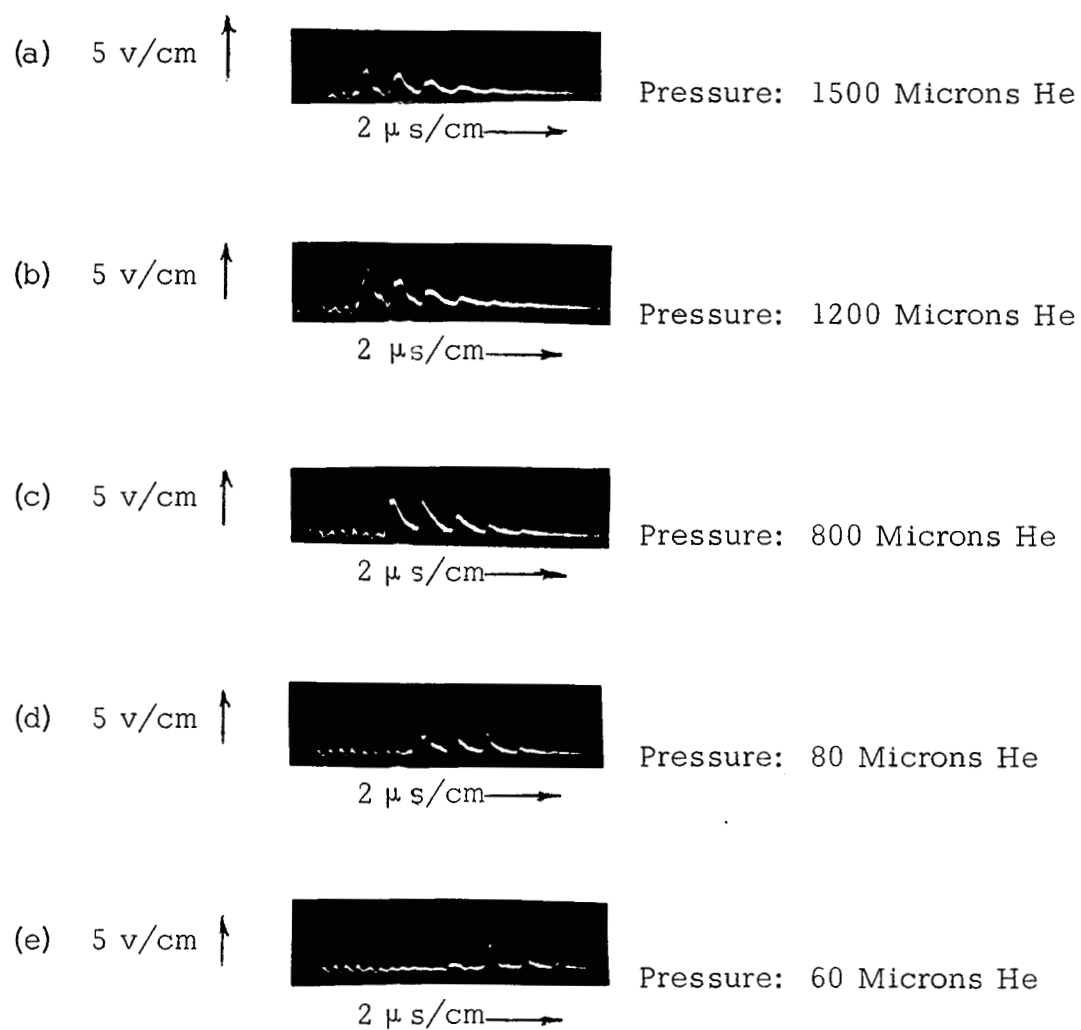
Fig.19. X-RAY PULSE SHAPE vs PRESSURE
WITH TESLA COIL PREIONIZATION

FIGURE 20.

AMPLITUDE vs. PRESSURE FOR RF AND TESLA COIL
PREIONIZATION.

Tesla Coil Preionization

RF Preionization

Pressure (Microns)

Amplitude (Arbitrary Units)

43

91 – A1862
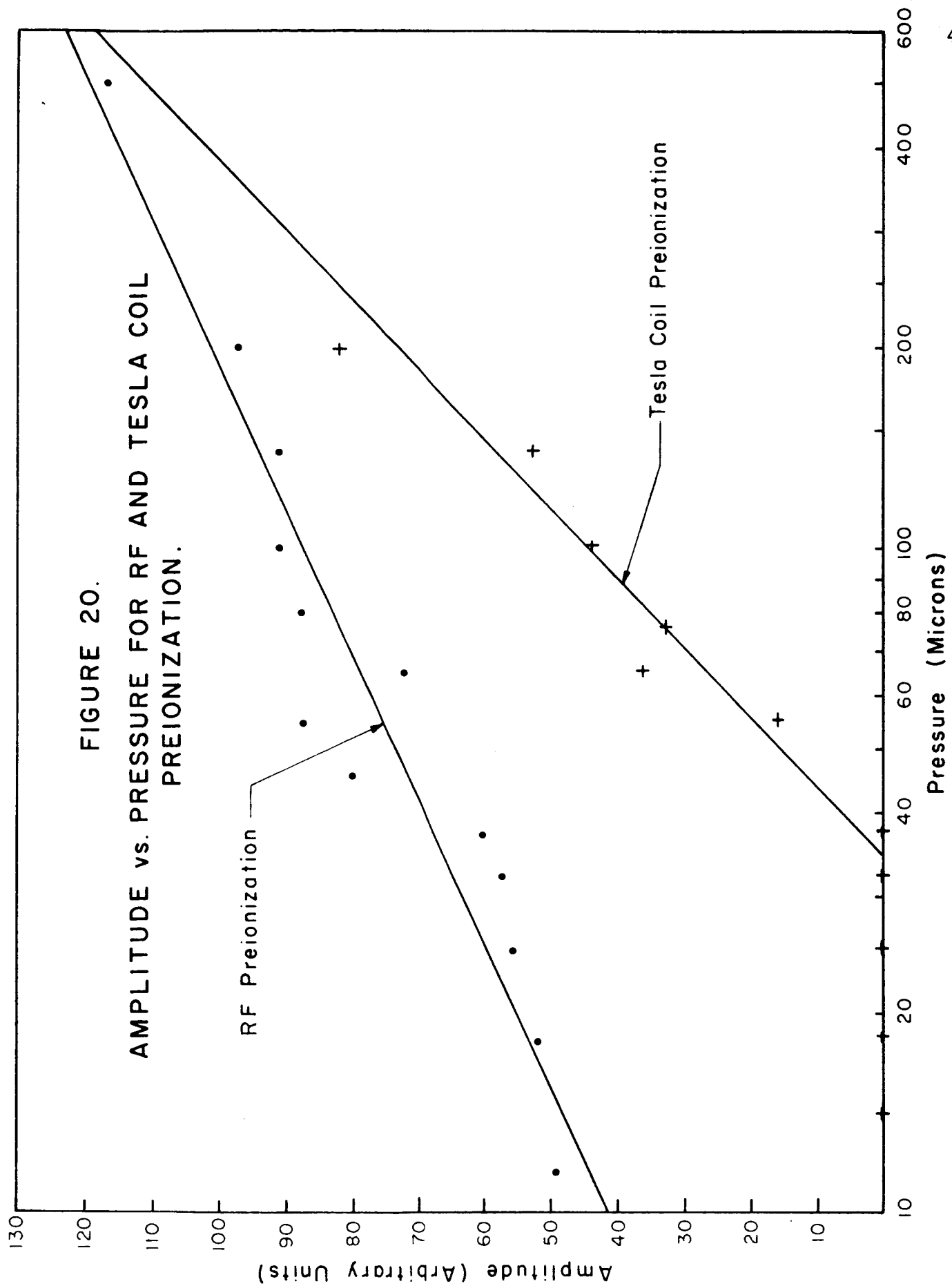
value close to the theoretically predicted value. A more thorough comparison of the pressure effect is possible with the assistance of Figure 20. In this figure, the effect of two types of preionization are also compared.

An experiment was performed comparing results from Tesla coil and RF preionization. Both forms of preionization were tested at a capacitor charging voltage of 19 KV. In order to get graphical results, it was arbitrarily decided to measure and total the peak heights of the two principal pulses for each trace. It was obvious that this technique would not give reliable quantitative results, but the results could be used as a qualitative indication of trend. These results indicate that RF preionization is more . effective in extending the range of operation of the plasma compression source.

4.3. X-Ray Spectra

Figure 21 illustrates typical x-ray spectra as obtained with a 1 meter grazing incidence vacuum spectrograph. The grating had a line density of 760 lines per mm. The slit width was approximately .0007", and the film used was Kodak SWR. Diaphine was used as the developer. Although it was found slower than the more conventional D-19, the results appeared cleaner and were favored for that reason.

The figure represents a typical spectrum taken at a pressure of 30 microns Hg where low helium purity exists because of very low flow rates. We have chosen these results for presentation here because they are more adaptable for photographic reproduction. The lines shown are largely impurity lines. Similar exposures taken in helium at 100 microns Hg showed results similar to those illustrated. Comparison of several spectra as a function of pressure indicated that the line intensity increased at the lower pressures. Presumably, this is due to plasma interaction with the compression tube walls which might be expected to be enhanced at lower pressures.

Increasing Wavelength

Fig. 21 . X-RAY SPECTRUM

FROM THE PLASMA COMPRESSION

Comparison of the spectra shown in Figure 21 with a spectrum obtained at a helium pressure of 100 microns showed several additional lines which are most likely the helium 200 Angstrom series. The spectra shown have not been calibrated. However, the region shown in this figure covers the spectrum between 100 and 400 Angstroms. The direction of increasing wavelength is indicated in the figure.

5. Conclusions

This program has led to the successful development of a prototype pulsed source of high intensity vacuum ultraviolet and soft x-radiation. The research which has been carried out has been oriented toward proving the concept of the plasma compression technique and establishing the operational parameters necessary for the final engineering design of the prototype.

The initial conceptual design for the source stemmed from an approximate analysis which predicted copious continuum and line emission from a compressed plasma with electron temperatures near 50 electron volts. An electrodeless pinch device has been constructed to produce such a plasma and performance has been monitored by two principle methods, i.e.: (1) time resolved observations of the non-dispersed radiation below about 1000 $\overset{o}{A}$ and (2) time integrated recording on film of the line radiation in the wavelength range 100 to 400 $\overset{o}{A}$.

In performing these measurements, the operational parameters and techniques have been optimized with regard to maximizing the radiation output and establishing reliable results. For example, the radiation dependence on gas pressure and method of preionization have been extensively studied. In the course of research several matters related to engineering design have also been treated. These relate to methods for switching the capacitor discharge, to differential pumping requirements and to means for obtaining critical alignment of the source.

The scope of the program has precluded source additional diagnostic measurements. These might include: absolute calibration of the source intensity, a full spectroscopic analysis of the line radiation and a determination of the plasma temperature, the specie density and the physical-chemical kinetics within the plasma. Based on the initial observations an investigation into these unexplored areas is strongly recommended for future study.

A finished prototype of the source is being completed as a final
product of this program. The source has been designed specifically
for use in conjunction with the JACO Ultraviolet Spectrograph at
the Goddard Space Flight Center. The final device has been
mechanically and electrically engineered to provide trouble-free service
and to incorporate many automatic features which facilitate operation.
To supplement the physical design characteristics summarized in this
report a manual is being prepared to describe the final instruments
operation and maintenance.

SCIENCES INCORPORATED